Liquid Li Structure and Dynamics: A Comparison Between OFDFT and Second Nearest-Neighbor Embedded-Atom Method

Mohan Chen
Dept. of Mechanical and Aerospace Engineering, Princeton University, Princeton, NJ 08544

Joseph R. Vella, Athanassios Z. Panagiotopoulos, and Pablo G. Debenedetti
Dept. of Chemical and Biological Engineering, Princeton University, Princeton, NJ 08544

Frank H. Stillinger
Dept. of Chemistry, Princeton University, Princeton, NJ 08544

Emily A. Carter
Dept. of Mechanical and Aerospace Engineering, Princeton University, Princeton, NJ 08544

Program in Applied and Computational Mathematics, Andlinger Center for Energy and the Environment, Princeton University, Princeton, NJ 08544

DOI 10.1002/aic.14795
Published online April 8, 2015 in Wiley Online Library (wileyonlinelibrary.com)

The structure and dynamics of liquid lithium are studied using two simulation methods: orbital-free (OF) first-principles molecular dynamics (MD), which employs OF density functional theory (DFT), and classical MD utilizing a second nearest-neighbor embedded-atom method potential. The properties studied include the dynamic structure factor, the self-diffusion coefficient, the dispersion relation, the viscosity, and the bond angle distribution function. Simulation results were compared to available experimental data when possible. Each method has distinct advantages and disadvantages. For example, OFDFT gives better agreement with experimental dynamic structure factors, yet is more computationally demanding than classical simulations. Classical simulations can access a broader temperature range and longer time scales. The combination of first-principles and classical simulations is a powerful tool for studying properties of liquid lithium. © 2015 American Institute of Chemical Engineers *AIChE J*, 61: 2841–2853, 2015
Keywords: transport, liquid lithium, diffusion, viscosity, density functional theory, computer simulations (MC and MD)

Introduction

Liquid metals have attracted considerable attention recently, due to their potential use as plasma-facing components in tokamak reactors.[1,2] Liquid lithium (Li) and its alloys, such as lithium-tin, show the greatest promise as plasma-facing components.[3,4] Simulation studies are a useful complement to experimental ones, particularly so for liquid metal systems that are difficult to study experimentally. For example, in the case of liquid Li, its comparatively high melting temperature of 453.7 K, when compared to organic materials, and its reactivity with water, pose experimental challenges that, although not insurmountable, make the availability of alternative approaches desirable. Various simulation methods exist, ranging from quantum mechanical approaches relying on density functional theory (DFT) to classical simulation techniques.

Kohn–Sham (KS) DFT[5,6] is a first-principles method based on quantum mechanics that can be used without empirical parameters. KSDFT for metallic systems is limited by its $O(N^3)$ scaling of time required to complete simulations, where N is the number of atoms being simulated. Because of this, KSDFT-based molecular dynamics (MD) methods are impractical when one wants to calculate properties that require computationally demanding simulations. For example, the calculation of viscosity requires a fairly large number of atoms and a simulation time long enough to see the smooth decay of an autocorrelation function.

Alternatively, orbital-free (OF) DFT is a quasi linear-scaling (at most $O(Nln(N))$) first-principles method based on quantum mechanics.[7] OFDFT is orders of magnitude less expensive than KSDFT, enabling the routine quantum simulation of many thousands of atoms.[8] This method has been used to study the liquid state of several materials such as aluminum[9] and magnesium.[10] It has recently been shown to be accurate enough to describe both solid and liquid properties of Li.[11] The melting point of Li as well as the diffusivity and static structure factors of the liquid phase were shown to agree well with experimental measurements.[11] However, with respect to the diffusivity, the effect of system size was

Mohan Chen and Joseph R. Vella contributed equally to the writing of this article.

Correspondence concerning this article should be addressed to P. G. Debenedetti at pdebene@princeton.edu.

not fully investigated in previous work; this will be fully addressed in this study.

In addition to first-principles methods, classical simulation methods have also been used to study Li and other metals. These methods are much less computationally expensive than quantum mechanical approaches. Therefore, they allow the simulation of tens of thousands of atoms over periods of hundreds of nanoseconds.[12] Classical simulation methods require the specification of a force field to describe interactions between atoms. A common class of force fields for simulating metals is the embedded-atom method (EAM) family of potentials.[13] These potentials are referred to as semiempirical because experimental and/or first-principles data are used to determine their parameters. Second nearest-neighbor modified embedded-atom method (2NN MEAM) potentials are a class of EAM potentials[14] that have been shown to be particularly well-suited for simulating metals that form a stable body-centered cubic (bcc) crystal.[15]

In this work, we employ both OFDFT-MD and classical MD (utilizing a 2NN MEAM potential) to study structural and dynamic properties of Li, with an emphasis on the liquid phase. Knowledge of structural and dynamic properties is of fundamental importance when considering a liquid metal as a possible plasma-facing component candidate. We validate these two methods by comparing results for various properties of Li to experimental data. This allows us to compare and contrast the two methods. In addition to liquid properties, we also examine the relative stability of different Li crystal structures and the surface energies of the bcc crystal. The properties of liquid Li obtained from our simulations that can be directly compared to experimental data include the dynamic structure factor, the self-diffusivity, the dispersion relation, and the viscosity. The simulations also provide the bond angle distribution function, for which no experimental data are available, to the best of our knowledge.

In this article, the "Models" Section describes both the OFDFT and 2NN MEAM treatment of Li. The "Methods" Section provides details of the simulation methods used to compute different properties of Li. The "Results" Section presents results of the simulations and compares them to available experimental data. In addition, we provide a performance assessment for both OFDFT and 2NN MEAM methodologies. Finally, the "Concluding Remarks" Section describes conclusions from our work.

Models

Orbital-free DFT

In OFDFT, the total energy of a given system is written as

$$E^{\mathrm{DFT}}[\rho(\mathbf{r})]=T_s[\rho(\mathbf{r})]+E_{\mathrm{H}}[\rho(\mathbf{r})]+E_{\mathrm{XC}}[\rho(\mathbf{r})]+E_{\mathrm{IE}}[\rho(\mathbf{r})]+E_{\mathrm{II}} \tag{1}$$

here $T_s[\rho(\mathbf{r})]$ is the kinetic energy density functional (KEDF), where $\rho(\mathbf{r})$ is the electron density in real space, $E_{\mathrm{H}}[\rho(\mathbf{r})]$ is the Hartree energy representing electron-electron Coulomb repulsion interactions, $E_{XC}[\rho(\mathbf{r})]$ is the electron exchange-correlation energy term, $E_{\mathrm{IE}}[\rho(\mathbf{r})]$ is the electron-ion energy term, and E_{II} is the ion–ion energy term that can be calculated using Ewald summation.[8,16]

Both KSDFT and OFDFT are founded upon the Hohenberg–Kohn theorems.[5,6] However, there exist two major differences between them. First, in KSDFT the kinetic energy term is expressed in terms of wave functions while OFDFT adopts a KEDF. For $T_s[\rho(\mathbf{r})]$, we use the Wang–Govind–Carter (WGC99) KEDF.[17] This is a nonlocal functional with a density-dependent kernel based on the Lindhard response function.[18] The WGC99 KEDF in real space has three terms (in atomic units)

$$\begin{aligned} T[\rho(\mathbf{r})]=&C_{\mathrm{TF}}\int \rho^{5/3}(\mathbf{r})d\mathbf{r}+\frac{1}{8}\int\frac{|\nabla\rho(\mathbf{r})|^2}{\rho(\mathbf{r})}d\mathbf{r}\\ &+C_{\mathrm{TF}}\int\int \rho^{\alpha}(\mathbf{r})\omega_{\alpha\beta\gamma}\left[\left(\frac{k^{\gamma}(\mathbf{r})+k^{\gamma}(\mathbf{r}')}{2}\right)^{1/\gamma},\mathbf{r}-\mathbf{r}'\right]\rho^{\beta}(\mathbf{r}')d\mathbf{r}d\mathbf{r}' \end{aligned} \tag{2}$$

where $C_{\mathrm{TF}}=\frac{3}{10}(3\pi^2)^{2/3}$. The first term of Eq. 2 is the Thomas–Fermi KEDF,[19–21] which is a local KEDF solely dependent on $\mathbf{r}$. The second term is the von Weizsäcker KEDF.[22] This is a semilocal KEDF due to the use of the density gradient $\nabla\rho(\mathbf{r})$. The WGC99 KEDF introduces a third, nonlocal term. Exponents α and β are set to $\alpha=\frac{5+\sqrt{5}}{6}$ and $\beta=\frac{5-\sqrt{5}}{6}$, in order to satisfy two physical limits. First, by enforcing $\alpha+\beta=5/3$, the nonlocal term is guaranteed to recover the uniform electron gas limit, that is, the Thomas–Fermi KEDF. Next, by enforcing $1-\frac{8}{9\alpha\beta}=-\frac{3}{5}$, the WGC99 KEDF also captures the large-q limit (where q is the wave vector) for rapidly varying densities.[17,23,24] The Fermi vector is $k(\mathbf{r})=[3\pi^2\rho(\mathbf{r})]^{1/3}$, where the exponent $\gamma=2.7$ is shown to work well for simple metals.[17] The density-dependent nonlocal kernel $\omega_{\alpha\beta\gamma}$ is obtained by solving a second-order differential equation, which is chosen to satisfy the Lindhard linear response relations at the uniform electron gas limit.[17,25] Using the nonlocal KEDF with a density-dependent kernel within OFDFT provides an accurate description of both bulk and surface properties of simple metals.[17,26] Here, nonlocal refers to a term with both $\mathbf{r}$ and $\mathbf{r}'$ variables. Utilizing the WGC99 KEDF, the OFDFT total energy is explicitly expressed as a functional of $\rho(\mathbf{r})$. The ground-state energy of a given system can be obtained by applying standard minimization methods to Eq. 1. Conversely, the kinetic energy term in KSDFT does not have an explicit functional form of $\rho(\mathbf{r})$. Minimization methods that are well suited for OFDFT cannot be used in KSDFT to find the ground-state energy. The total energy in KSDFT is usually obtained by diagonalizing the Hamiltonian matrix (the scaling for the diagonalization method is $O(N^3)$) expressed in wave functions, which makes KSDFT several orders of magnitude slower than OFDFT.[8]

The second difference between the two methods comes from the treatment of the ion-electron interaction term, $E_{\mathrm{IE}}[\rho(\mathbf{r})]$, in Eq. 1. The pseudopotential approximation is widely used in electronic structure theory. A pseudopotential is an effective potential that replaces the all-electron potential of an atom.[27] The influence of core electrons are included in the pseudopotential, leaving only the valence electrons to be treated. Using a pseudopotential instead of an all-electron potential increases the efficiency of KSDFT because a reduced number of plane wave basis functions can be used to describe the orbitals and operators. Nonlocal pseudopotentials[28] are constructed by dividing the pseudopotential into a local pseudopotential and a set of nonlocal projectors. The nonlocal projectors are designed to act on orbitals. However, OFDFT cannot use nonlocal pseudopotentials due to its lack of orbitals. In this study, a bulk-derived local pseudopotential[29,30] for Li is used instead of a nonlocal

pseudopotential. The validation of bulk-derived local pseudopotentials for solid and liquid states of Li has been discussed in previous work.[11]

For $E_{XC}[\rho(\mathbf{r})]$, we adopt the generalized gradient approximation in the Perdew–Burke–Ernzerhof (PBE)[31] form. All the OFDFT simulations are performed using the PRinceton Orbital-Free Electronic Structure Software (PROFESS) package.[32–34] A 900-eV kinetic energy cutoff is used for the plane wave basis expansion, and periodic boundary conditions are used.

2NN MEAM potential

We used the 2NN MEAM potential for Li developed by Cui et al.[35] As mentioned earlier, one reason for choosing this potential is because the 2NN MEAM class of potentials has been shown to perform well for materials that form a stable bcc crystal phase.[15] Additionally, our recent study has shown that this particular Li potential is the best among five alternative Li EAM potentials.[36] In particular, this potential was shown to give the best agreement with the zero pressure melting point, and was successful in predicting saturated liquid densities and liquid-phase radial distribution functions without using liquid-phase data during the parameter fitting procedure. The parameters of this potential were obtained using a variety of solid properties such as elastic constants, unrelaxed surface energies, unrelaxed vacancy energies, and the binding energies of crystal structures as well as three molecular structures (Li_2, Li_3, Li_4).[35] While the data for the first two properties were taken from experiments, the rest of the properties were taken from first-principles calculations. We note that the first-principles calculations for the three molecular structures utilized the PBE treatment of the exchange-correlation term. Note that the same form of exchange-correlation term is used in OFDFT-MD simulations.

The potential energy of the system described by the 2NN MEAM potential is given by

$$E_{\text{pot}}^{\text{2NNMEAM}} = \sum_j F_j(\phi_j) + \frac{1}{2}\sum_j \sum_{k\neq j} \varphi_{jk}(r_{jk}) \tag{3}$$

In the above expression, F_j is the embedding energy, a function of the effective electron density ϕ_j at the site of atom j. This term is a many-body term and can be thought of as the energy it takes to embed atom j into a background electron density ϕ_j caused by surrounding atoms. The embedding energy is typically viewed as accounting for metallic bonding. The second term, $\varphi_{jk}(r_{jk})$, is a pair potential, which accounts for effective electrostatic interactions and r_{jk} is the distance between atoms j and k. All the 2NN MEAM calculations are done with the LAMMPS molecular dynamics package[12] (http://lammps.sandia.gov; September 30, 2013 version) using periodic boundary conditions.

Methods

Although the focus of this work is on liquid properties of Li, we briefly address the performance of each method for the prediction of selected properties of solid Li. Specifically, we chose to examine the relative stability of four crystal structures of Li. These are the body-centered cubic (bcc), face-centered cubic (fcc), simple cubic (sc), and diamond (dia) structures. Out of these crystal structures, only bcc and fcc are known to appear on the phase diagram of Li.[37] We also studied the surface energies of bcc Li, the stable phase under ambient conditions.

In all OFDFT and classical MD simulations of liquid Li, a time step of 0.5 fs was used. Unless otherwise specified, a 1024-atom cell size was used. The mass of the natural abundance of Li was used, corresponding to an assignment of $m = 6.941$ atomic mass units to all atoms.

Solid Li

Close to 0 K, it has been shown experimentally that Li has a close-packed rhomobohedral 9R crystal structure.[38] However, bcc is the most stable structure under ambient conditions. During our comparison between the OFDFT and 2NN MEAM simulations, we do not consider the rhomobohedral 9R crystal structure.

In the OFDFT simulations, the electron density optimization problem of various crystal structures of Li at 0 K was defined on a uniform three-dimensional grid in real space. A steepest descent algorithm is used for cell optimizations; all the cell vectors were allowed to vary independently during the cell optimizations. At each cell optimization step, the ion positions are fixed at their positions determined by their space group symmetry, while a truncated Newton algorithm[32] was used to optimize electron density to find the ground-state energy. For 2NN MEAM calculations, the energies and equilibrium volumes of various crystal structures of Li at 0 K were found by performing an energy minimization by varying atom coordinates and the box dimensions using a steepest descent algorithm.

We examined the surface energies for different surfaces of the Li bcc crystal, specifically the bcc (100), (110), and (111) surfaces. The surface energy E_s is defined here as[30]

$$E_s = \frac{E_{\text{slab}} - NE_0}{2A} \tag{4}$$

where E_{slab} is the total energy of a periodic slab with a relaxed geometry and in-plane lattice vectors fixed at those optimized for bulk bcc Li, N is the number of atoms, E_0 is the energy per atom of bulk bcc Li, and A is the area of the surface under consideration. The factor of 2 accounts for the two surfaces of the slab. Equation 4 is used to calculate the relaxed surface energies in both OFDFT and classical calculations. For OFDFT, the ion relaxation was performed using the conjugate-gradient algorithm as implemented in PROFESS[32] while for classical simulations a steepest-descent algorithm was used. Seven layers of Li were used to ensure convergence of surface energies.

Liquid density

All liquid properties were calculated in the canonical (constant NVT) ensemble. However, before this was done we needed to ensure the densities in the simulations were chosen such that they were at zero pressure. We did this by performing preliminary simulations in the isothermal-isobaric (constant NPT) ensemble.

In the OFDFT-MD simulations, liquid densities at zero pressure and various temperatures were calculated using a 1024-atom cell. The Nosé–Hoover thermostat[39,40] and Parinello–Rahman[41] barostat were used. By monitoring the potential energy, we found that an interval of 15 ps was sufficient to reach equilibrium. We deemed a system to be in equilibrium when we saw that the potential energy fluctuated without drifting about a time-independent average value. The

fluctuations in potential energy were no more than 0.06% of the average value. This was followed by a 30-ps long production run to collect statistics. The liquid densities were then calculated by taking samples every 2.5 fs during the 30 ps production run.

Liquid densities at zero pressure for the classical simulations were calculated using a 6750-atom cell using the Nóse–Hoover thermostat[39,40] and Nóse–Hoover barostat.[42,43] It was found that an initial period of 1.5 ns was more than enough to reach equilibrium. Fluctuations of the potential energy during the production runs were no more than 0.4% of the average value. This was followed by a 1-ns long production period to collect statistics on the liquid density at a given temperature. The liquid densities were then calculated by taking samples every 20 fs during the production run.

We would like to briefly point out that we observe larger fluctuations in potential energy with the 2NN MEAM model as compared to OFDFT. The origin of this seems to be a difference in heat capacity between the two models, which can be calculated from fluctuations in the total energy of the system. However, in this work, we have not rigorously investigated this. It may be interesting to study the difference between the two models with respect to this property in the future, as well as the comparison to experimental data.

Dynamic structure factor

The dynamic structure factor, $S(q,\omega)$, contains information on the collective dynamics of density fluctuations over both length and time scales. Here, ω is frequency and the wave vector q is defined as the length of

$$\mathbf{q}=2\pi\left(\frac{n_1}{L_1},\frac{n_2}{L_2},\frac{n_3}{L_3}\right) \tag{5}$$

where L_1, L_2, and L_3 are the lengths of the lattice vectors of a given simulation cell, and n_1, n_2, and n_3 are non-zero integers. For all simulations performed in this work, we have $L_1=L_2=L_3$ because we utilized a cubic simulation box. The lengths of lattice vectors depend on the liquid density. As shown in the "Results" Section, the liquid density values calculated from OFDFT and classical MD simulations are nearly identical. Therefore, the same set of q vectors in both simulations are used.

Experimentally, $S(q,\omega)$ can be measured by inelastic neutron or inelastic x-ray scattering experiments.[44] Thus, the dynamic structure factor calculated from OFDFT and classical MD simulations can be directly compared to experimental results. $S(q,\omega)$ is defined as the Fourier transform with respect to time of the intermediate scattering function $I(q, t)$, which is defined as

$$I(q,t)=\frac{1}{N}\left\langle\left(\sum_{j=1}^{N}e^{-i\mathbf{q}\cdot\mathbf{r}_j(t+t_0)}\right)\left(\sum_{k=1}^{N}e^{-i\mathbf{q}\cdot\mathbf{r}_k(t_0)}\right)\right\rangle \tag{6}$$

where t is time, t_0 is the starting time, $\mathbf{r}_j$ and $\mathbf{r}_k$ are the atomic coordinates of atoms j and k respectively.

The system in OFDFT-MD simulations was equilibrated for 30 ps, followed by a 50-ps production trajectory. For classical MD simulations, the system was equilibrated for 1 ns, followed by a 1-ns production period. For OFDFT-MD simulations, fluctuations in potential energy during the production run were found to be no more than 0.06% of the average potential energy, while for classical MD simulations the fluctuations were no more than 0.6%. In both methods, configurations after every 2.5 fs were used to calculate the dynamic structure factor. For comparison purposes, we also performed a 50-ps production period in classical MD simulations and found that the resulting dynamic structure factors are almost identical to the ones from the 1 ns production period, indicating the dynamic structure factors at these selected q vectors are converged within 50 ps. In the following discussions, the calculated properties from classical MD simulations are analyzed based on the 1 ns trajectory unless otherwise specified.

Self-diffusivity

For both types of simulations, the calculated self-diffusion coefficient D^{calc} was obtained using the Einstein relation

$$D^{\text{calc}}=\frac{1}{6}\lim_{t\to\infty}\frac{d}{dt}\langle\Delta r(t)^2\rangle \tag{7}$$

Here, $\langle\Delta r(t)^2\rangle$ is the mean squared displacement of atoms at time t.

For OFDFT-MD simulations, three different cell sizes with 250, 686, and 1024 atoms were used at temperatures ranging from 470 to 620 K, in order to investigate the effect of cell size on the calculated diffusion coefficient. For the 1024-atom cell, we used the trajectory described in the section on calculation of the dynamic structure factor. For the other two cells, we used the same procedure that was used for 1024-atom cell; that is, first we equilibrate the system for 30 ps, followed by a 50-ps production run. In all simulations, the fluctuations of the potential energy during the production run were smaller than 0.2% of the average potential energy.

For the classical MD simulations, we examined five different cell sizes at temperatures ranging from 470 to 1000 K with 250, 686, 1024, 2662, and 6750 atoms. A 10 ns-long production period was run after an initial equilibration period for all simulations. For all systems a 1-ns long equilibration period was more than enough time to reach equilibrium. Fluctuations in potential energy during the production period never exceeded 1.7% of the average value for all simulations. Three to five independent runs were performed in order to obtain sufficient statistics.

Viscosity and dispersion relation

We utilized two methods for calculating the viscosity of liquid Li, namely, the transverse current autocorrelation function method and a Green–Kubo relation. The dispersion relation is computed from the longitudinal current autocorrelation function, as discussed below.

Transverse Current Autocorrelation Function. A current function is defined as

$$\mathbf{j}(q,t)=\sum_{j=1}^{N}\mathbf{v}_j(t)e^{i\mathbf{q}\cdot\mathbf{r}_j(t)} \tag{8}$$

where $\mathbf{v}_j(t)$ is the velocity of atom j and $\mathbf{r}_j(t)$ is the position of atom j at time t. $\mathbf{j}(q,t)$ can be divided into two parts

$$\mathbf{j}(q,t)=j_l(q,t)+j_t(q,t). \tag{9}$$

Here, $j_l(q,t)$ is the longitudinal component of $\mathbf{j}(q,t)$ parallel to wave vector $\mathbf{q}$, and $j_t(q,t)$ is the transverse component of $\mathbf{j}(q,t)$ perpendicular to wave vector $\mathbf{q}$. The current autocorrelation functions are defined in terms of their longitudinal and transverse components

$$C_l(q,t)=\frac{1}{N}\langle j_l(q,t)j_l(q,0)\rangle \tag{10}$$

$$C_t(q,t)=\frac{1}{N}\langle j_t(q,t)j_t(q,0)\rangle \tag{11}$$

The Fourier transform of the time domain of $C_l(q,t)$ is $C_l(q,\omega)$, which satisfies the condition: $C_l(q,\omega)=\omega^2 S(q,\omega)$. A well-defined side peak can be observed in $C_l(q,\omega)$. The dispersion relation can then be obtained by plotting the frequency of the side peak from $C_l(q,\omega)$ as a function of q. The dispersion relation can also be directly compared to inelastic x-ray or neutron scattering experiments. In the small q region where q is approaching the hydrodynamic limit, the q-dependent adiabatic sound velocity can be calculated from the dispersion relation and it becomes the bulk adiabatic sound velocity at $q=0$.

For OFDFT-MD simulations, the viscosity was calculated using the transverse current autocorrelation function.[45] This method has been used in prior studies.[9,10] The formula to derive the shear viscosity using this method is

$$C_t(q,t)=\frac{k_B T}{m}\exp\left[-\frac{q^2\eta(q)t}{m\rho}\right] \tag{12}$$

where k_B is the Boltzmann constant, T is temperature, m is the mass corresponding to the natural abundance of Li in atomic mass units, and ρ is the liquid number density. After performing an integration over t for $C_t(q,t)$, we obtain the formula for the shear viscosity

$$\eta(q)=\frac{k_B T\rho}{q^2 C_t(q,\omega=0)} \tag{13}$$

The shear viscosity η was obtained by extrapolating $\eta(q)$ to the hydrodynamic limit ($q\rightarrow 0$ Å^{-1}) using the formula proposed by Palmer[45]

$$\eta(q)=\eta+aq^2 \tag{14}$$

where η is the viscosity in the hydrodynamic limit and a is a fitting parameter. Because the systems we studied have inversion symmetry upon q, this implies that $\eta(q)$ must be an even function of q. We used q vectors greater than 0.7 Å^{-1} to fit Eq. 14 and obtained the final viscosity of liquid Li for different temperatures. We also applied this method for classical MD simulations to compare to the Green–Kubo relation described in the next section. We used the same data and statistical analysis methods as for the dynamic structure factor calculations.

Green–Kubo Relation. For the classical MD simulations, shear viscosity was calculated using a Green–Kubo relation which relates the shear viscosity to the integral of the stress autocorrelation function[46]

$$\eta=\frac{V}{k_B T}\int_0^\infty \langle P_{xy}(0)P_{xy}(t)\rangle\ dt \tag{15}$$

Here, k_B is the Boltzmann constant, T is temperature, V is the volume, and $P_{xy}(t)$ are values of the off-diagonal components of the stress tensor at time t. One can obtain improved statistics in the calculation of viscosity by including all components of the stress tensor.[47] The relation is then adjusted to the following equation[48]

$$\eta=\frac{V}{10k_B T}\int_0^\infty \left(\sum_{\alpha\beta}\langle P_{\alpha\beta}(0)P_{\alpha\beta}(t)\rangle\right)\ dt \tag{16}$$

where $\alpha\beta=xx,xy,xz,yx,yy,yz,zx,zy,$ and zz. In the above equation, we have

$$P_{\alpha\beta}=(\pi_{\alpha\beta}+\pi_{\beta\alpha})/2-\delta_{\alpha\beta}\left(\sum_\gamma \pi_{\gamma\gamma}\right)/3 \tag{17}$$

where $\delta_{\alpha\beta}$ is the Kronecker delta and

$$\pi_{\alpha\beta}=\frac{1}{V}\left[\sum_j m_j v_{j\alpha}v_{j\beta}+\sum_j\sum_{k>j}(r_{j\alpha}-r_{k\alpha})f_{jk\beta}\right] \tag{18}$$

Here, m_j is the mass of atom j, and $v_{j\alpha}$ and $v_{j\beta}$ are the α and β components of the velocity of atom j. $r_{j\alpha}$ and $r_{k\alpha}$ are the α components of the position vectors of atom j and atom k and $f_{jk\beta}$ is the β component of the force on atom j due to atom k.

Calculations of viscosity using the 2NN MEAM potential used the same set of simulations as the diffusion coefficient calculations.

Bond angle distribution function

The bond angle distribution function, $g_{3,r_c}(\theta)$, is a quantity used to characterize the local structure of liquid systems. For each atom j in a simulation cell at each temperature, r_c is the finite radius that includes the two nearest neighbors of atom j. Note that the value of r_c varies for each atom j due to the different locations of its nearest neighbors. θ is defined as the angle between two vectors joining atom j and its two nearest neighbors. We chose a bin width of $\theta=0.1^\circ$. We used the same set of simulations as the dynamic structure factor calculations.

Results

Solid Li

Table 1 displays the energy differences between various crystal structures of Li and the bcc crystal phase at 0 K. We also list the equilibrium volumes for each of the crystal structures studied. In addition to the predictions made by OFDFT and classical simulations, results from KSDFT[11] and any available experimental data are also shown. Table 1 also contains the surface energies of the bcc crystal calculated from Eq. 4.

In terms of the energy orderings of the crystal structures, we can see that the OFDFT results reproduce the KSDFT results very well. Both predict fcc and bcc to be nearly degenerate and lower energy than any of the other crystal structures studied. The classical treatment predicts the bcc crystal to be the most stable at 0 K among the crystal structures studied. The energy differences between sc and bcc for all three computational approaches agree well. For the energy difference between dia and bcc, the agreement between the three is reasonable. We also see good agreement for the equilibrium volumes between all three computational methods, aside from the hypothetical diamond structure. Its four-coordinate motif is challenging to describe within the 2NN MEAM and OFDFT formalisms.

The most stable surface of the bcc crystal predicted by both OFDFT and classical calculations is the (110) surface. This contradicts the result from KSDFT, which predicts the (100) surface to be the most stable. However, the energy difference between Li bcc (110) and (100) is small (at most 51 mJ/m^2) for all three types of calculations, and it is known that the most stable surfaces of bcc metals are in fact these two facets.

Liquid density

For both OFDFT and classical MD simulations, the calculated liquid densities for different temperatures at zero pressure are shown in Table 2.

Table 1. Comparison of Solid Properties of Li

Property	System	KSDFT	OFDFT	Classical	Exp.
ΔE (eV/atom)	$\Delta E_{bcc \to fcc}$	−0.002	−0.001	0.012	−0.0011[49]
	$\Delta E_{bcc \to sc}$	0.121	0.150	0.144	
	$\Delta E_{bcc \to dia}$	0.394	0.427	0.527	
V (Å^3/atom)	bcc	20.354	20.207	20.626	21.63[50a]
	fcc	20.318	20.266	20.624	
	sc	20.509	21.948	19.904	
	dia	25.798	30.328	22.152	
E_s (mJ/m^2)	bcc (100)	465	438	422	
	bcc (110)	492	412	371	522,[51] 525[52b]
	bcc (111)	549	507	514	

We display results from KSDFT, OFDFT, and classical simulations. ΔE is the calculated energy difference between a specified crystal structure and bcc structure of Li, V is the equilibrium volume, and E_s is the surface energy. All DFT results are from Ref. [11]. Available experimental data are also included.

[a]Experimental volume at 294 K.

[b]These values are not assigned to any particular surface.

The data in the first row of Table 2 were used for subsequent OFDFT-MD simulations while the values in the second row were used for classical MD simulations in order to simulate the bulk liquid at zero pressure in the NVT ensemble. From these simulations, we were able to calculate a variety of structural and dynamic properties of liquid Li.

In general, we can see liquid densities from the two simulation methods agree well with experimental data. We note that the experimental data shown in Table 2 were taken from a linear fit to the raw data found in the references. The liquid densities from OFDFT-MD are slightly lower than those calculated from classical MD and experimental data.[53,54] The difference between the liquid densities predicted from OFDFT-MD and the other datasets becomes larger at higher temperatures. This may due to the fact that the WGC99 KEDF and bulk-derived local pseudopotentials begin to exhibit errors as the liquid expands and becomes less "nearly free-electron-like" at higher temperatures. We note that the agreement between the predicted liquid densities from classical MD simulations using the Cui 2NN MEAM potential and experimental data is consistent with the results of our previous study of classical Li potentials.[36]

Dynamic structure factor

Figure 1 shows the normalized intermediate scattering function $I(q, t)$ from both OFDFT and classical MD simulations for several q vectors. The values of q shown are 0.72, 1.24, and 3.53 Å^{-1}. For each q value, we show $I(q, t)$ at two different temperatures, namely, 470 and 620 K.

For a given type of simulation and at a given value of q, we see similar behavior in all $I(q, t)$ for both temperatures. All $I(q, t)$ decay quickly and vanish after approximately 1.0 ps. The peaks for the intermediate scattering functions at 620 K are smoother than those at 470 K, indicating that correlations are weaker for liquid Li at higher temperatures. For $q = 3.53$ Å^{-1}, the OFDFT results agree very well with the classical results for both amplitudes and peak positions. However, there are some discrepancies between the OFDFT and classical results at q values of 0.72 and 1.24 Å^{-1}, where the classical results have a significantly larger amplitude than the OFDFT results. We also found that the results obtained from 50 ps and 1 ns trajectories using classical simulations are almost identical for all three q vectors. This indicates that a 50-ps trajectory is long enough to get a sufficiently converged intermediate scattering function.

Table 2. Temperature Dependence of the Density of Liquid Li (in g/cm^3)

Methods	470 K	520 K	570 K	620 K
First-Principles	0.5066	0.5001	0.4939	0.4876
Classical	0.5098	0.5051	0.5005	0.4960
Exp. (Novikov et al.[53])	0.5157	0.5117	0.5054	0.5002
Exp. (Yakimovich et al.[54])	0.5124	0.5077	0.5028	0.4981

We display results from OFDFT and classical MD simulations. Two sets of experimental data are also included.

The dynamic structure factors of liquid Li at 470 K are shown in Figure 2. Results from OFDFT and classical MD simulations are compared to experimental data.[44]

There are several important observations to note from these results. First, in general, the OFDFT results provide better agreement with experimental data than the classical results. However, it can be seen that the classical results agree better with experimental results at small values of ω with the exception of the dynamic structure factor at $q = 1.24$ Å^{-1}. The dynamic structure factor obtained from classical simulations agrees well at $q = 3.53$ Å^{-1} with both experiment and OFDFT simulations. We note that the OFDFT-MD results yield good agreement with the location and amplitude of the second peak when compared to experiment for $q = 0.72$ Å^{-1} and $q = 1.24$ Å^{-1}. At these q values, the classical results underestimate the location of the peaks by about 10 ps^{-1} and also overestimate the magnitude of the peaks in $S(q, \omega)$ by about 0.5×10^{-3} ps.

Self-diffusivity

As mentioned in the "Methods" Section, several different cell sizes were examined in order to investigate the size-dependence of the calculated self-diffusion coefficient. The calculated self-diffusion coefficients D^{calc} for different cell sizes (as a function of the inverse of the simulation box length) from both OFDFT and classical MD simulations are shown in Figure 3.

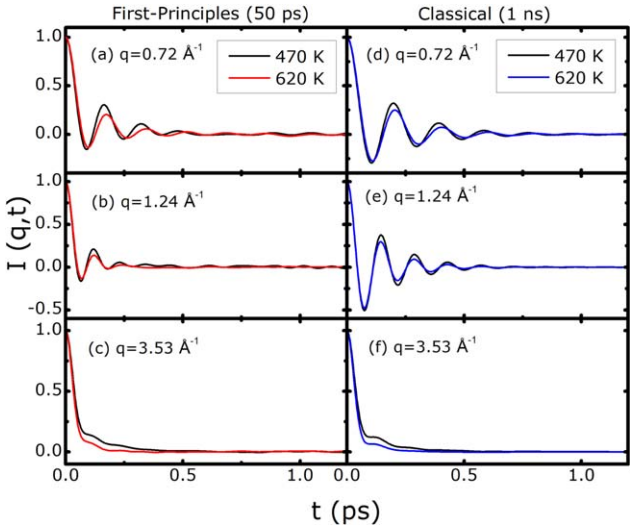

Figure 1. Intermediate scattering function $I(q, t)$ for liquid Li.

The left column shows results from 50 ps long OFDFT-MD simulation trajectories at 470 K and 620 K at three different q vectors. The right column shows results from 1 ns long classical MD simulation trajectories at 470 and 620 K at three different q vectors.

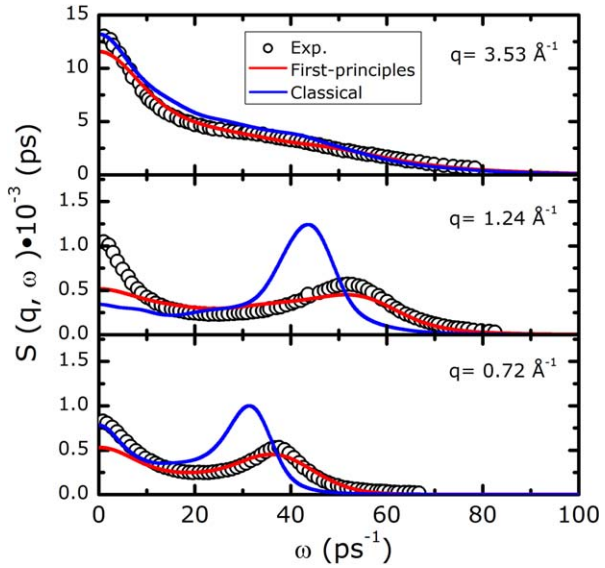

Figure 2. Dynamic structure factor $S(q,\omega)$ of liquid Li at 470 K.

We display experimental results[44] and results from OFDFT and classical MD simulations.

It is clear that D^{calc} depends on the size of the cell for both methods. To obtain a self-diffusion coefficient D^{extr} that does not have an artificial size effect, a weighted linear regression is performed on D^{calc} as a function of inverse simulation box length at each temperature. Each point is weighted by the inverse of its variance. D^{extr} is obtained from an extrapolation of D^{calc} to infinite cell size ($\frac{1}{L} \rightarrow 0$ Å^{-1}). After we obtained D^{extr}, we went back to each D^{calc} and applied a correction which accounts for cell-size effects in simulations with periodic boundary conditions given by Yeh and Hummer.[55] The corrected self-diffusion coefficient D^{corr} is written as

$$D^{corr} = D^{calc} + \frac{k_B T \xi}{6\pi\eta L} \tag{19}$$

Here, k_B is the Boltzmann constant, T is temperature, ξ is a constant equal to 2.837297, η is the viscosity, and L is the length of the simulated cubic cell. For η, we use the values calculated from simulations discussed in the next section. In Figure 3, D^{corr} are shown as filled symbols at each cell size. It is clear that the corrected values agree well with D^{extr}, therefore validating the correction scheme for both simulation types.

D^{extr} from both OFDFT and classical MD simulations are presented in Figure 4. Experimental data are also shown for comparison.[56] As illustrated in Figure 4, both simulation results agree well with each other for temperatures up to 620 K. They also agree with the experimental results in this temperature range. The classical simulations were performed at temperatures up to 1000 K. The classical simulations continue to give excellent agreement with experimental data, which extends to 830 K.

For the OFDFT-MD simulations using the 1024-atom cell, we found that a numerical instability exists at systems with temperatures higher than 620 K. This instability can occur during an MD trajectory and prohibit the correct ground-state energy and forces from being obtained. As stated earlier, the WGC99 KEDF is based on Lindhard linear response theory, which is exact for a uniform electron gas and very accurate for light metals. However, when a simulation cell has localized electrons (which can occur in systems containing covalent bonds, atoms in close proximity, or isolated atoms), this KEDF is inappropriate and does not perform well. Specifically, in spatial regions where the electron density is highly nonuniform and/or very low, as could be expected at higher temperatures, the WGC KEDF can give infinitely deep kinetic potentials in the self-consistent loop used to converge the electron density. Here, we see that the total energy from the self-consistent loop diverges. This divergence may be due to the truncated (second-order) Taylor expansion of the WGC response kernel used to achieve the quasilinear scaling of the OFDFT computation.[17] This problem prohibited us from performing the OFDFT-MD simulations at higher temperatures. A similar issue was observed when applying the same KEDF for a silicon diamond structure.[57]

Viscosity and dispersion relation

The viscosity results calculated by the transverse current autocorrelation function method and the Green–Kubo relation are presented below. Figure 5 shows the transverse current autocorrelation functions $C_t(q,t)$ from OFDFT and classical simulations using four different values of q: 0.22, 0.72, 1.24, and 3.53 Å^{-1}.

Two lengths of trajectory are used: 50 ps and 1 ns. We did not perform a 1-ns trajectory with OFDFT-MD simulations because the calculation is too expensive. For the three values of q, excluding q= 0.22 Å^{-1}, there is good agreement between OFDFT and classical simulations. Also, as can be seen from Figure 5, the transverse autocorrelation functions from both the 50 ps (green line) and 1 ns (blue dashed line) trajectories using classical methods are almost

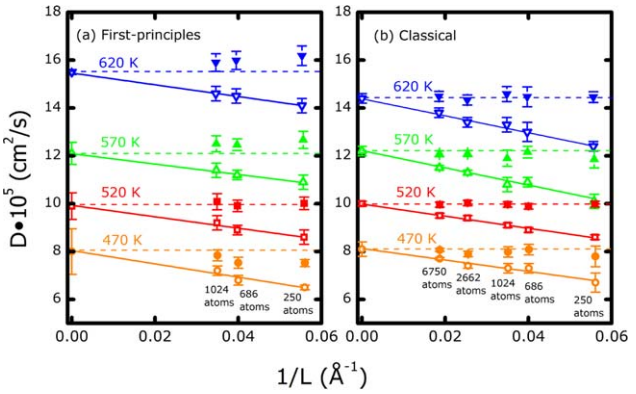

Figure 3. Self-diffusion coefficient of liquid Li at ambient pressure and at 470, 520, 570, and 620 K from (a) OFDFT and (b) classical MD simulations for different cell sizes.

The solid lines are lines of best fit from a weighted linear regression. The horizontal dashed lines correspond to the self-diffusion coefficient in the hydrodynamic limit D^{extr}. The open symbols are the calculated self-diffusion coefficient D^{calc} taken directly from simulations, while filled symbols are the values of the self-diffusion coefficient D^{corr} using the cell size correction proposed by Yeh et al. (see Eq. 19).[55] For both first-principles and classical simulations, error bars represent the 95% confidence interval calculated from independent simulations.

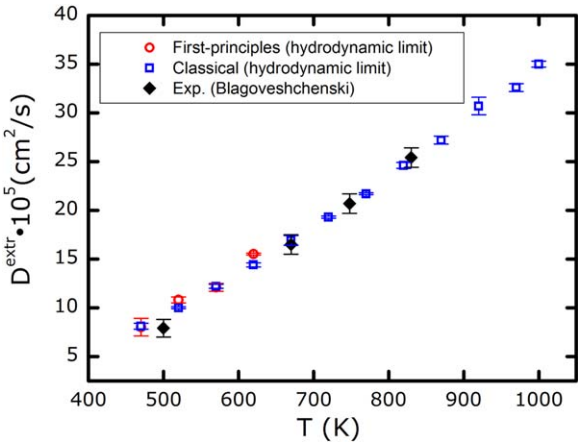

Figure 4. Self-diffusion coefficients D^{extr} from extrapolation method using OFDFT and classical simulations compared to experimental data.

Experimental data from Blagoveshchenskii et al.[56] are also shown. For the simulation data, the error bars represent the 95% confidence interval taken from the extrapolation to infinite system size (see Figure 3).

indistinguishable, indicating a 50-ps trajectory is long enough to obtain a converged $C_t(q,t)$ at these three q vectors. However, for the smallest q value in Figure 5a, only the $C_t(q,t)$ from the 1 ns trajectory smoothly decays after 1 ps. This indicates a 50-ps trajectory at $q = 0.22$ Å^{-1} is not long enough to obtain a converged $C_t(q,t)$. Furthermore, we conclude that $C_t(q,t)$ is difficult to converge as the hydrodynamic limit ($q \to 0$ Å^{-1}) is approached.

The q dependence of the calculated viscosity is shown in Figure 6.

Here, we use 50 ps trajectories for the OFDFT simulation and 1 ns trajectories for the classical simulation. Both simulation methods show the same dependence of the calculated viscosity with respect to q. From Figure 6, we are able to extract the value of viscosity in the hydrodynamic limit. At low values of q, the data from the classical simulation is less noisy when compared to the data from the other simulation. This is because the viscosity at each q is calculated from longer trajectories for the classical simulation. This is consistent with the conclusions drawn from Figure 5.

We were also able to obtain the dispersion relation from longitudinal current autocorrelation functions. The dispersion relation for liquid Li at 470 and 620 K from both simulation methods and experimental data[44,58] are shown in Figure 7.

Both simulation methods are in very good qualitative agreement. However, there are noticeable discrepancies between the two sets of experimental data. The data from de Jong et al.[58] have large uncertainties, while the data from Sinn et al.[44] provide smaller uncertainties and encompass a wider range of q. The OFDFT-MD simulation results agree well with the experimental results from Sinn et al.[44] The classical simulation results give quantitatively comparable results to OFDFT results except for q vectors ranging from 0.5 to 2.2 Å^{-1}, with the largest difference observed at approximately $q = 1.5$ Å^{-1}. The experimental sound velocity in bulk Li at 470 K (4550 m/s)[59] is shown as a black solid line in Figure 7. Both simulation results match the experimental sound velocity as the hydrodynamic limit is approached.

Next, we discuss the viscosity calculated from the Green–Kubo relation. Figure 8 shows the stress autocorrelation function of liquid Li at a few temperatures calculated from classical simulations.

It is clear that the function decays within 1 ps. Results from first-principles simulations are not shown because the

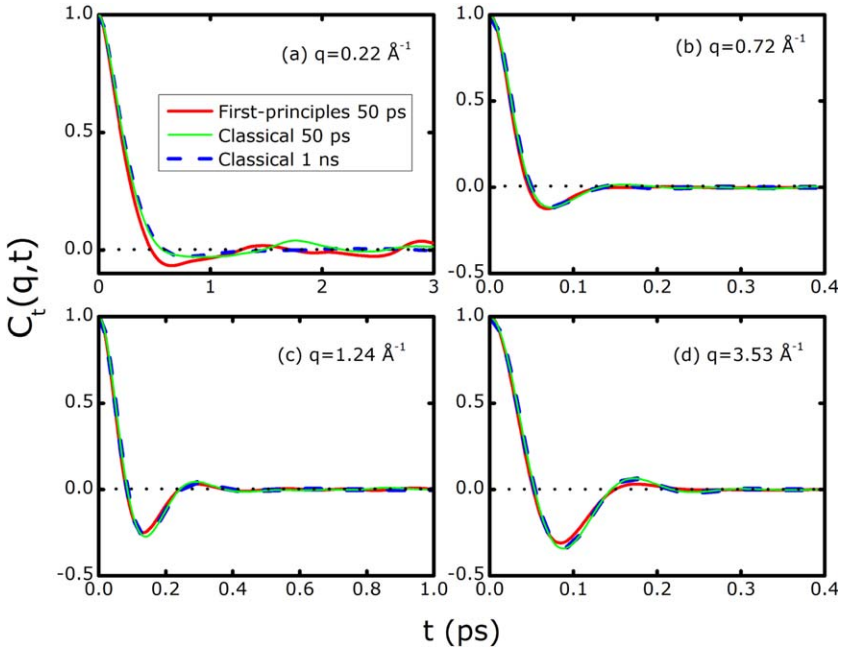

Figure 5. Transverse current autocorrelation functions $C_t(q,t)$ for liquid Li at 470 K.

The red line is from a 50-ps OFDFT-MD simulation. The green line is from a 50-ps classical MD simulation and the blue dashed line is from a 1-ns classical MD simulation. Plots (a), (b), (c), and (d) use a q of 0.22 Å^{-1}, 0.72 Å^{-1}, 0.124 Å^{-1}, and 3.53 Å^{-1} respectively.

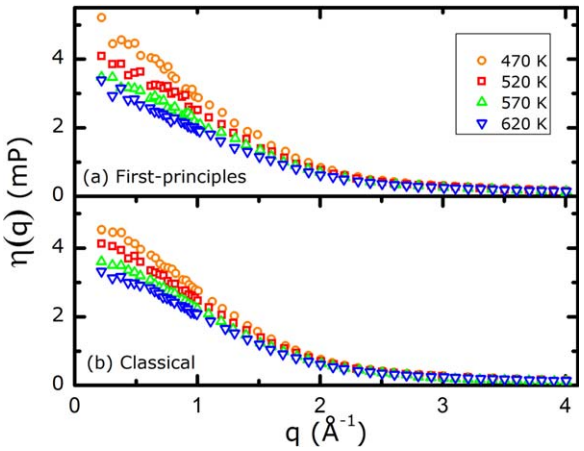

Figure 6. Calculated q dependent viscosity $\eta(q)$ for liquid Li at 470, 520, 570, and 620 K.

Plot (a) shows results from OFDFT-MD simulations and plot (b) shows results from classical MD simulations.

Green–Kubo formalism was not applied for these simulations. Although the decay time of the stress autocorrelation functions for first-principles simulations was similar to the classical simulations, a long trajectory is still needed to obtain sufficient statistics. As mentioned in the "Methods" Section, the classical simulations used a 10-ns production period to collect statistics on the stress autocorrelation function. This length of time cannot be easily reached in first-principles simulations. Therefore, even though the stress tensor can be calculated from the first-principles simulations, we did not apply the Green–Kubo relation to these simulations.

The effect of cell size on the calculated viscosity using the Green–Kubo relation for classical simulations is shown in Figure 9.

We used the same set of cell sizes mentioned in the self-diffusion coefficient section, that is, 250, 686, 1024, 2662, and 6750-atom cells. Analogous calculations for first-principles simulations using the transverse current autocorrelation function were not performed for two reasons. First, due to the relatively short trajectories of the first-principles

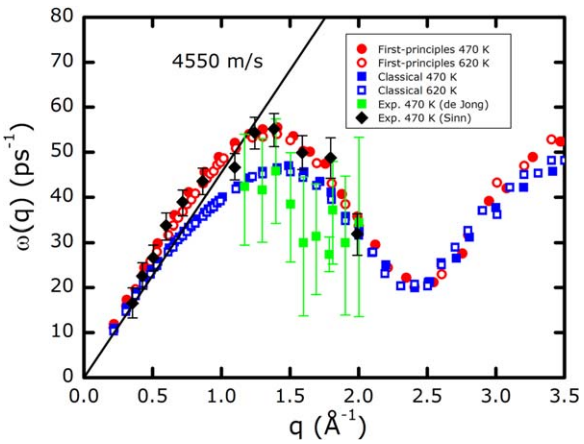

Figure 7. The calculated dispersion relation for liquid Li at 470 and 620 K from OFDFT and classical simulations.

The black line represents the bulk adiabatic sound velocity (4550 m/s) at 470 K from experiment.[59] Experimental data from de Jong et al.[58] and Sinn et al.[44] are also shown.

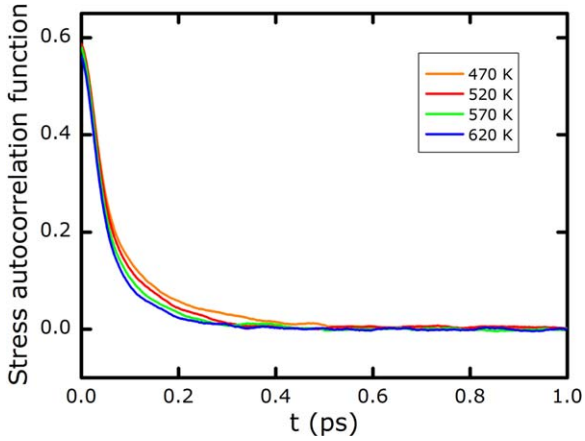

Figure 8. Stress autocorrelation function for liquid Li from classical simulations at 470, 520, 570, and 620 K.

simulations, the calculated viscosity has a larger uncertainty when compared to those obtained from classical simulations. Therefore, the size effect for viscosity cannot be accurately studied with first-principles simulations. Second, it is much more computationally demanding to simulate larger cells using first-principles simulations than using classical simulations. It is clear that the effect of cell size on the calculation of viscosity is less pronounced when compared to the calculation of the diffusion coefficient. The data show that the calculated viscosities become statistically indistinguishable once a certain cell size is reached. From Figure 9, it seems that the viscosity converges for cell sizes of 686 atoms and larger. We can therefore come to the conclusion that the viscosity has negligible size effects in the 6750-atom cell (the largest cell we examined when calculating viscosity), from which we choose to take the converged viscosity. The final results for viscosity are plotted in Figure 10.

The simulation results are compared to available experiment data.[60–63] The OFDFT results (red circles) are taken from the transverse current autocorrelation function methodology, while the classical results (blue squares) are taken from the Green–Kubo relation. As mentioned earlier, we compared the values of viscosity from classical simulations calculated using the transverse current autocorrelation

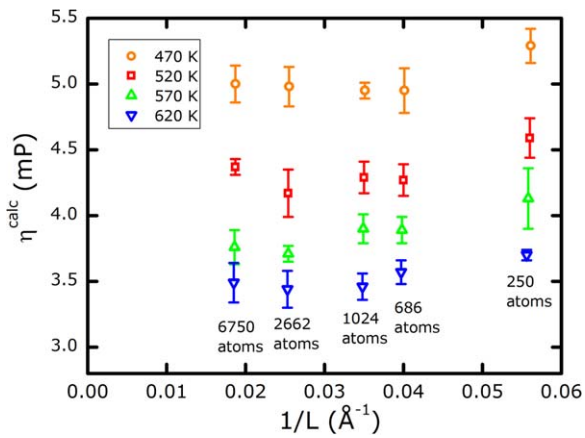

Figure 9. Cell size dependence of the calculated viscosity of liquid Li from classical simulations.

The error bars represent the 95% confidence interval calculated from independent simulations.

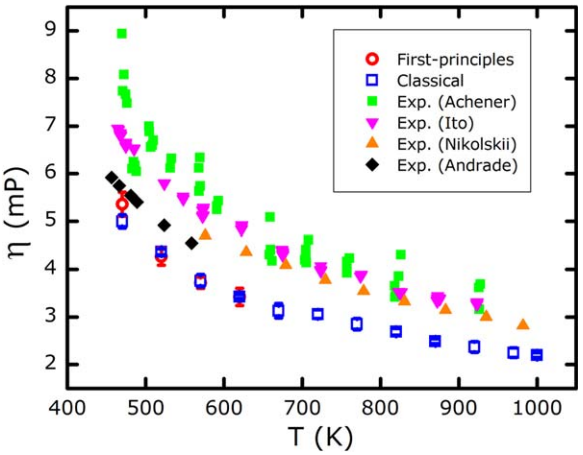

Figure 10. Calculated viscosity of liquid Li from OFDFT and classical MD simulations.

Experimental data[60–63] are also displayed. For the first-principles simulations, error bars represent the 95% confidence interval calculated by fitting $\eta(q)$ for $q>0.7$ in Figure 6 to Eq. 14 (polynomial fit) and extrapolating to the hydrodynamic limit. For the classical simulations, error bars represent the 95% confidence interval calculated from independent simulations.

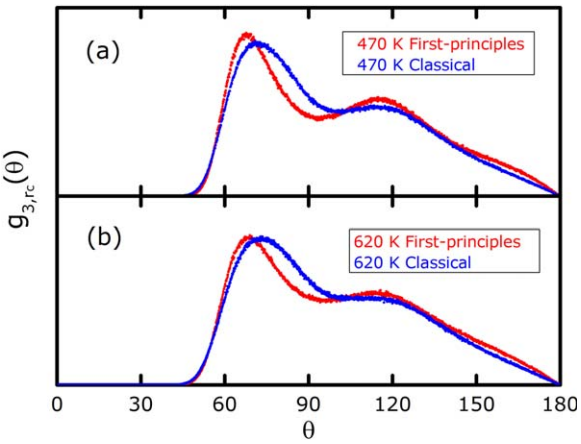

Figure 11. Calculated bond angle distribution functions $g_{3,r_c}(\theta)$ of liquid Li from OFDFT and classical MD simulations at 470 K (a) and 620 K (b).

function method to the values using the Green–Kubo treatment for several temperatures. We show the comparison in Table 3. We find that the calculated viscosities show good agreement between the two methods. This illustrates the equivalence between the two methods.

As was the case for the self-diffusion coefficient, we observe excellent agreement between the viscosity calculated from both simulation methods. The agreement with experimental data is reasonable, however, it is not as good as the agreement of the predicted self-diffusivity with experiment. The calculated viscosities are about 20% smaller than experimental data from Andrade.[63] Because the viscosity data given by Andrade are systematically lower than those obtained from the other studies shown, we point out that our simulation predictions give worse agreement with the other datasets plotted in Figure 10. It should be noted that there is a significant spread in the experimental data. There can be several reasons for this. For example, Ito et al.[61] mention that the disagreement may be due to a difference in theories for extracting the viscosity from experiments, or because corrosion at the walls of the experimental apparatus used in certain studies may have influenced measurements. Both simulation methods capture the temperature dependence of the viscosity. This is made clear by examining the results from classical simulations which extend to 1000 K.

Bond angle distribution function

In Figure 11, we compare the bond angle distribution functions from both simulation methods at 470 and 620 K.

Table 3. Viscosity (in mP) from the Transverse Current Autocorrelation Function Method and Green–Kubo Relations for Classical Simulations

Method	470 K	520 K	570 K	620 K
Transverse current autocorrelation function	4.89 ± 0.09	4.52 ± 0.08	3.83 ± 0.05	3.45 ± 0.06
Green–Kubo	5.00 ± 0.14	4.37 ± 0.06	3.76 ± 0.13	3.43 ± 0.04

As stated earlier, as far as we know, there are no experimental data to compare to the simulation results. Both methods yield similar bond angle distribution functions. From Figure 11, we can see that both simulation methods display two peaks at both temperatures. All bond angle distribution functions rise at approximately $\theta=45^{\circ}$ and smoothly go to zero at $\theta=180^{\circ}$. Both methods capture the correct trend that at higher temperatures the peaks tend to become wider and smoother. However, there are some differences between the results obtained from the two methods. The two peak positions of the bond angle distribution functions from OFDFT simulations are around $\theta=67^{\circ}$ and $\theta=114^{\circ}$ while for classical simulations they are located around $\theta=72^{\circ}$ and $\theta=117^{\circ}$. We also observe that bond angle distribution functions from classical simulations are slightly higher than those from OFDFT simulations between the two peaks. However, we assert that the bond angle distribution functions for both simulations methods agree reasonably well.

Performance assessment

A performance assessment for both simulation methods can provide useful information on the relative computational cost of each method. Three different sizes were chosen: 128, 1024, and 11,664-atom cells. Table 4 compares the wall time per MD step for both methods.

The OFDFT-MD simulations were carried out by PROFESS 3.0[34] and classical MD simulations were carried out by the LAMMPS package (http://lammps.sandia.gov).[12] All wall times were obtained by averaging 10,000 MD steps. Both simulations were performed on nodes with two Intel

Table 4. Wall Time (in s) for each MD Step Carried Out by OFDFT and Classical Simulations

Method	Number of Processors	128 Atoms	1024 Atoms	11,664 Atoms
First-Principles	1	3.6	32	N/A
	8	0.70	6.8	130
	16	0.48	4.1	71
Classical	1	0.0025	0.019	0.22
	8	0.00073	0.0030	0.029
	16	0.00061	0.0019	0.015

Three different sample sizes of liquid Li were used: 128, 1024, and 11,664 atom cells.

Xeon E5–2670 @ 2.60 GHz, where each node has 16 GB RAM.

Several points can be drawn from Table 4. First, both methods scale almost linearly with system size, between 128 and 11,664 atoms. Second, we obtain excellent speedup in both methods when increasing the number of processors to 16. Third, although the OFDFT simulations used in this study are already several orders of magnitude faster than simulations that utilize KSDFT, the classical simulations are about three orders of magnitude faster than the OFDFT simulations. Therefore, it is not surprising that classical simulations can easily reach MD trajectory time scales that are on the order of tens of ns, while OFDFT-MD simulations are only able to easily obtain results over time scales that are on the order of tens of ps. It should be noted that for the largest cell size (11,664 atoms), OFDFT simulations run into memory limitations on a single processor with 2 GB of memory.

Concluding Remarks

In this article, we presented a comprehensive study of Li using both first-principles (OFDFT) and classical (2NN MEAM force field) MD. We briefly examined solid Li structures and then focused on structural and dynamic properties of liquid Li. For solid Li, we looked at the relative stability and equilibrium volumes of various crystal structures at 0 K. We also examined the surface energies of bcc Li. We compared our results to KSDFT calculations and available experimental data. The properties of liquid Li we studied include the dynamic structure factor, the self-diffusion coefficient, the dispersion relation, the viscosity, and the bond angle distribution function. For the first four of these, we compared results from both simulation methods to the available experimental data. This allowed us to comment on the accuracy of each method. For the case of the bond angle distribution function, we were only able to compare the two simulation methods to each other because of the lack of experimental data. Comparing first-principles and classical simulations allowed us to examine the advantages and disadvantages of each method.

For solid Li, we found that both methods generally give good agreement with the KSDFT results in terms of the relative stability of crystals and equilibrium volumes. However, both OFDFT and the 2NN MEAM potential predict the (110) face of the bcc crystal to be the most stable. This contradicts KSDFT calculations.

For the dynamic structure factor, when compared to the experimental data,[44] first-principles simulations are generally more accurate than classical simulations. With respect to the self-diffusion coefficient, we have shown that there is a dependence on the system size for the calculated value for both simulation methods. Both show a linear relationship between the calculated self-diffusion coefficient and the inverse of the simulation box length. By simulating several system sizes and extrapolating to the hydrodynamic limit ($\frac{1}{L} \rightarrow 0$ Å^{-1}), we were able to obtain the self-diffusion coefficient without size effects. The values calculated from both simulation methods agree well with each other and also match experimental data within the temperature range 470–620 K. The classical simulations are able to access higher temperatures, and in fact we continued to see agreement with experimental data as we increased the temperature. For the dispersion relation, we found that the first-principles simulation calculations gave excellent agreement with experimental data. Classical simulations showed noticeable deviations with respect to experiments, however, they were able to yield good agreement in the hydrodynamic limit. Viscosity was calculated from the transverse current autocorrelation function for OFDFT simulations and from a Green–Kubo relation for classical simulations. Both methods give good agreement with one another, but they underestimate the values with respect to experiment. However, they do seem to capture the qualitative dependence of viscosity on temperature. We compared the bond angle distribution function given by the two simulation methods at two different temperatures. We found that there is generally good agreement between both methods. Finally, we performed benchmark calculations to emphasize the difference in the cost of computing resources between both simulation methods. We showed that the classical simulations are approximately three orders of magnitude faster than OFDFT simulations.

This study enables us to make recommendations concerning which simulation method to use when studying selected properties of liquid Li. Although both simulation methods gave similar results for the self-diffusion coefficient and viscosity, we recommend that the classical simulations be used when these properties are important. We claim this for two reasons. The first is that classical simulations are computationally less demanding than first-principles simulations, which is clearly shown by the performance assessment. Therefore, one is able to simulate larger systems over longer time scales when this method is employed. Second, although the WGC99 KEDF gives the most accurate description for simple metals near their melting points, it suffers from divergence problems at significantly higher temperatures. This limits the temperature range for which that functional can be used to study liquid Li. Classical simulations are not restrained in this respect.

In spite of the above considerations, there are still properties in which first-principles simulations outperform classical simulations. As stated earlier, this is shown to be the case for the dynamic structure factor and the dispersion relation. In studies where these properties are important, it would therefore be advantageous to use the first-principles simulations given that they yield better agreement with experimental data. For example, in addition to providing a convenient comparison to experimental measurements, it has been suggested that analysis of the dynamic structure factor for liquid alkali metals may aid in identifying the presence of the metal–nonmetal transition, which takes place near the liquid–vapor critical point.[64] The dispersion relation is useful for obtaining the bulk adiabatic sound velocity, as we demonstrated in this work. First-principles simulations also provide a good comparison with classical simulations for properties where experimental data are not readily available. This was the case for the bond angle distribution functions of liquid Li.

This work emphasizes an important relationship between quantum mechanical simulation methods, such as OFDFT simulations, and classical simulations. While there are advantages and disadvantages associated with each method, they can be used together in order to obtain a better understanding of a wide range of materials and properties. As stated earlier, 2NN MEAM force fields contain parameters that need to be fitted using either experimental data or first-principles calculations, as is the case for many classical force fields. In the absence of experimental data, comparison with

first-principles calculations is the most reliable way to fit parameters of empirical force fields. Therefore, OFDFT calculations (as well as other quantum mechanical approaches such as KSDFT) should be used to fit 2NN MEAM (or other classical) potentials for systems where experimental data are scarce. Indeed, future work will focus on systems in which this is the case. This includes systems such as hydrogen/deuterium–lithium mixtures and various lithium alloys.

Acknowledgments

The authors thank the Office of Fusion Energy Science, U.S. Department of Energy, which provided support for this work under Award DE-SC0008598. EAC would like to acknowledge additional financial support from the Office of Naval Research (Grant No. N00014-11-1-0137). The authors also thank Beatriz Gonzalez del Rio for helpful discussions on dynamic properties and viscosity calculations and Zhiwei Cui for helpful comments on solid-phase calculations using the 2NN MEAM potential. The authors acknowledge the Terascale Infrastructure for Groundbreaking Research in Science and Engineering (TIGRESS) high performance computing center at Princeton University and the Innovative and Novel Computational Impact on Theory and Experiment (INCITE) project for computational resources.

Literature Cited

1. Hassanein A, Allain JP, Insepov Z, Konkashbaev I. Plasma/liquid-metal interactions during tokamak operation. *Fusion Sci Technol*. 2005;47:686–697.
2. Coenen JW, De Temmerman G, Federici G, Philipps V, Sergienko G, Strohmayer G, Terra A, Unterberg B, Wegener T, Vanden Bekerom DCM. Liquid metals as alternative solution for the power exhaust of future fusion devices: Status and perspective. *Phys Scr*. 2014;2014:014037.
3. Majeski R. Liquid metal walls, lithium and low recycling boundary conditions in tokamaks. *AIP Conf Proc*. 2010;1237:122–137.
4. Allain JP, Ruzic DN, Hendricks MR. D, He, and Li sputtering of liquid eutectic Sn-Li. *J Nucl Mater*. 2001;290–293:33–37.
5. Hohenberg P, Kohn W. Inhomogeneous electron gas. *Phys Rev*. 1964;136:B864–B871.
6. Kohn W, Sham LJ. Self-consistent equations including exchange and correlation effects. *Phys Rev*. 1965;140:A1133–A1138.
7. Wang YA, Carter EA. Orbital-free kinetic energy density functional theory. In: Schwartz SD, editor. *Theoretical Methods in Condensed Phase Chemistry. Progress in Theoretical Chemistry and Physics*. Dordrecht: Kluwer, 2000:117–184.
8. Hung L, Carter EA. Accurate simulations of metals at the mesoscale: explicit treatment of 1 million atoms with quantum mechanics. *Chem Phys Lett*. 2009;475:163–170.
9. González DJ, González LE, López JM, Stott MJ. Dynamical properties of liquid Al near melting: an orbital-free molecular dynamics study. *Phys Rev B*. 2002;65:184201.
10. Sengül S, González DJ, González LE. Structural and dynamical properties of liquid Mg. An orbital-free molecular dynamics study. *J Phys: Condens Matter*. 2009;21:115106.
11. Chen M, Hung L, Huang C, Xia J, Carter EA. The melting point of lithium: an orbital-free first-principles molecular dynamics study. *Mol Phys*. 2013;111(22–23):3448–3456.
12. Plimpton S. Fast parallel algorithms for short-range molecular dynamics. *J Comput Phys*. 1995;117:1–19.
13. Daw MS, Baskes MI. Embedded-atom method: derivation and application to impurities, surfaces, and other defects in metals. *Phys Rev B*. 1983;29:6443–6453.
14. Lee B, Baskes MI. Second nearest-neighbor modified embedded-atom-method potential. *Phys Rev B*. 2000;62:8564–8567.
15. Lee B, Baskes MI, Kim H, Cho YK. Second nearest-neighbor modified embedded atom method potential for BCC transition metals. *Phys Rev B*. 2001;64:181402.
16. Ewald PP. Die berechnung optischer und elektrostatischer gitterpotentiale. *Ann Phys*. 1921;369:253–287.
17. Wang YA, Govind N, Carter EA. Orbital-free kinetic-energy density functionals with a density-dependent kernel. *Phys Rev B*. 1999; 60(24):16350–16358.
18. Lindhard J. On the properties of a gas of charged particles. *Dan. Mat. Fys. Medd*. 1954;28:8.
19. Thomas LH. The calculation of atomic fields. *Math Proc Cambridge Philos Soc*. 1927;23:542–548.
20. Fermi E. Un metodo statistico per la determinazione di alcune prioprietá dell'atomo. *Rend Accad Naz Lincei*. 1927;6:602–607.
21. Fermi E. Eine statistische berundung zur bestimmung einiger eigenshaften des atoms und ihre anwendungen auf die theorie des periodischen systems der elemente. *Z Phys*. 1928;48:73–79.
22. von Weizsäcker CF. Zur theorie der kernmassen. *Z Phys*. 1935;96: 431–458.
23. Wang YA, Govind N, Carter EA. Orbital-free kinetic-energy density functionals for the nearly free electron gas. *Phys Rev B*. 1998; 58(20):13465–13471.
24. Wang YA, Govind N, Carter EA. Erratum: orbital-free kinetic-energy density functionals for the nearly free electron gas [Phys. Rev. B 58, 13465 (1998)]. *Phys Rev B*. 2001;64:129901–1–129901-2.
25. Ho G, Ligneres VL, Carter EA. Analytic form for a nonlocal kinetic energy functional with a density-dependent kernel for orbital-free density functional theory under periodic and Dirichlet boundary conditions. *Phys Rev B*. 2008;78:045105.
26. Ho G, Huang C, Carter EA. Describing metal surfaces and nanostructures with orbital-free density functional theory. *Curr Opin Solid State Mater Sci*. 2008;11:57.
27. Hamann DR, Schlüter M, Chiang C. Norm-conserving pseudopotentials. *Phys Rev Lett*. 1979;43:1494–1497.
28. Kleinman L, Bylander DM. Efficacious form for model pseudopotentials. *Phys Rev Lett*. 1982;48:1425–1428.
29. Zhou B, Wang YA, Carter EA. Transferable local pseudopotentials derived via inversion of the Kohn–Sham equations in a bulk environment. *Phys Rev B*. 2004;69:125109.
30. Huang C, Carter EA. Transferable local pseudopotentials for magnesium, aluminum and silicon. *Phys Chem Chem Phys*. 2008;10:7109–7120.
31. Perdew JP, Burke K, Ernzerhof M. Generalized gradient approximation made simple. *Phys Rev Lett*. 1996;77:3865–3868.
32. Ho GS, Ligneres VL, Carter EA. Introducing PROFESS: a new program for orbital-free density functional theory calculations. *Comput Phys Commun*. 2008;179:839–854.
33. Hung L, Huang C, Shin I, Ho GS, Ligneres VL, Carter EA. Introducing PROFESS 2.0: a parallelized, fully linear scaling program for orbital-free density functional theory calculations. *Comput Phys Commun*. 2010;181:2208–2209.
34. Chen M, Xia J, Huang C, Dieterich JM, Hung L, Shin I, Carter EA. Introducing PROFESS 3.0: An advanced program for orbital-free density functional theory molecular dynamics simulations. *Comput Phys Commun*. 2015;190:228–230.
35. Cui Z, Gao F, Cui Z, Qu J. Developing a second nearest-neighbor modified embedded atom method interatomic potential for lithium. *Modell Simul Mater Sci Eng*. 2012;20:015014.
36. Vella JR, Stillinger FH, Panagiotopoulos AZ, Debenedetti PG. A comparison of the predictive capabilities of the embedded-atom method and modified embedded-atom method potentials for lithium. *J Phys Chem B*. In press. doi:10.1021/jp5077752
37. Guillaume CL, Gregoryanz E, Degtyareva O, McMahon MI, Hanfland M, Evans S, Guthrie M, Sinogeikin SV, Mao HK. Cold melting and solid structures of dense lithium. *Nat Phys*. 2011;7: 211–214.
38. Overhauser AW. Crystal structure of lithium at 4.2 K. *Phys Rev Lett*. 1984;53:64–65.
39. Nosé S. A unified formulation of the constant temperature molecular dynamics methods. *J Chem Phys*. 1984;81:511–519.
40. Hoover WG. Canonical dynamics: equilibrium phase-space distributions. *Phys Rev A*. 1985;31:1695–1697.
41. Parrinello M, Rahman A. Crystal structure and pair potentials: a molecular-dynamics study. *Phys Rev Lett*. 1980;45:1196–1199.
42. Hoover WG. Constant-pressure equations of motion. *Phys Rev A*. 1986;34:2499–2500.
43. Melchionna S, Ciccotti G, Holian BL. Hoover NPT dynamics for systems varying in shape and size. *Mol Phys*. 1993;78:533–544.
44. Sinn H, Sette F, Bergmann U, Halcoussis Ch, Krisch M, Verbeni R, Burkel E. Coherent dynamic structure factor of liquid lithium by inelastic X-ray scattering. *Phys Rev Lett*. 1997;78:1715–1718.

45. Palmer BJ. Transverse-current autocorrelation-function calculations of the shear viscosity for molecular liquids. *Phys Rev E*. 1994;49: 359–366.
46. Hansen J, McDonald I. *Theory of Simple Liquids*, 2nd ed. Waltham, MA: Academic Press, 1986.
47. Daivis PJ, Evans DJ. Comparison of constant pressure and constant volume nonequilibrium simulations of sheared model decane. *J Chem Phys*. 1994;100:541–547.
48. Lee SH, Chang T. Viscosity and diffusion constants calculation of n-alkanes by molecular dynamics simulations. *Bull Korean Chem Soc*. 2003;24:1590–1598.
49. Saunders N, Miodownik AP, Dinsdale AT. Metastable lattice stabilities for the elements. *CALPHAD*. 1988;12:351–374.
50. Anderson M, Swenson CA. Experimental equations of state for cesium and lithium metals to 20 kbar and the high-pressure behavior of the alkali metals. *Phys Rev B*. 1985;31:668–680.
51. Tyson WR, Miller WA. Surface free energies of solid metals: estimation from liquid surface tension measurements. *Surf Sci*. 1977;62: 267–276.
52. de Boer FR, Boom R, Mattens WCM, Miedema AR, Nissen AK. *Cohesion in Metals: Transition Metal Alloys*, 2nd ed. Amsterdam, North Holland: North Holland, 1988.
53. Novikov II, Trelin YS, Tsyganova TA. Experimental data on the speed of sound in lithium up to 1000°K. *Teplofiz Vys Temp*. 1969;7: 1220–1221.
54. Yakimovich KA, Mozgovoi AG. Experimental investigation of the density and surface tension of molten lithium at temperatures up to 1300 K. *High Temp*. 2000;38:657–659.
55. Yeh IC, Hummer G. System-size dependence of diffusion coefficients and viscosities from molecular dynamics simulations with periodic boundary conditions. *J Phys Chem B*. 2004;108:15873–15879.
56. Blagoveshchenskii NM, Noikov A, Savostin V. Self-diffusion in liquid lithium from coherent quasielastic neutron scattering. *Physica B*. 2012;407:4567–4569.
57. Zhou B, Ligneres V, Carter EA. Improving the orbital-free density functional theory description of covalent materials. *J Chem Phys*. 2005;122:044103.
58. de Jong PHK, Verkerk P, deGraaf LA. Collective modes at very short wavelengths in liquid lithium. *J Non-Cryst Solids*. 1993;156–158:48–52.
59. Canales M, González LE, Padró J. Computer simulation study of liquid lithium at 470 and 843 K. *Phys Rev E*. 1994;50:3656–3669.
60. Achener PY, Fisher DL. Viscosity of liquid sodium and lithium. *Technical Report*. AGN-8191. Aerojet-General Corporation, 1967.
61. Ito Y, Minami K, Nagashima A. Viscosity of liquid lithium by an oscillating-cup viscometer in the temperature range 464–923 K. *Int J Thermophys*. 1989;10:173–182.
62. Nikol'skii NA, Kalakutskaya NA, Pchelkin IM, Klassen TB, Vel'tishchva VA. *Teploenergetika*. 1959;2:92.
63. da C Andrade EN, Dobbs ER. The viscosities of liquid lithium, rubidium and caesium. *Proc R Soc A*. 1952;211:12–30.
64. Winter R, Pilgrim WC, Hensel F. The metal-non-metal transition and the static and dynamic structure factor of expanded liquid alkali metals. *J Phys: Condens Matter*. 1994;6:A245–A248.

Manuscript received Dec. 20, 2014, and revision received Mar. 13, 2015.